

1
2
3
4
5 1 **A new discrete element model for simulating a flexible ring net**
6
7 2 **barrier under rockfall impact comparing with large-scale physical**
8
9 **model test data**
10
11
12 4
13
14
15 5
16
17

18 6 **Zhuo-Hui Zhu, Jian-Hua Yin^{*}, Jie-Qiong Qin, Dao-Yuan Tan**
19
20

21 7
22
23
24 8
25
26 9 *Department of Civil and Environmental Engineering, The Hong Kong Polytechnic University,*
27
28 10 *Hung Hom, Kowloon, Hong Kong, China*
29
30

31 11
32
33 12
34
35
36 13 * Corresponding author.

37
38 14 *E-mail address: cejhyin@polyu.edu.hk (J.H. Yin).*
39 15
40
41 16
42
43
44 17
45
46 18
47
48
49 19
50
51 20
52
53
54 21
55
56
57 22
58

59 23 July 2019
60
61

1
2
3
4
5
6
7
8
9
10
11
12
13
14
15
16
17
18
19
20
21
22
23
24
25
26
27
28
29
30
31
32
33
34
35
36
37
38
39
40
41
42
43
44
45
46
47
48
49
50
51
52
53
54
55
56
57
58
59
60
61
62
63
64
65

24 **ABSTRACT**

25 Flexible barriers are one of the effective mitigation measures to intercept high-energy falling
26 rocks in mountainous areas, owing to its high ductility and excellent energy dissipation
27 performance. This paper presents a newly developed flexible ring net barrier model based on the
28 discrete element method (DEM) to simulate the rockfall impact on a flexible barrier. All the
29 input mechanical parameters were calibrated by means of laboratory tests. The capabilities of the
30 numerical model are evaluated by comparing the results from novel designed large-scale
31 physical model impact tests. It is found that the new discrete element model is able to reproduce
32 the behavior of a ring net barrier under rockfall impact. A good agreement with experimental
33 data can be found regarding to boulder velocities, net elongations and tensile forces developed
34 between ring net elements. In addition, the effects of boulder size, impact position, barrier
35 inclination, and barrier initial slack on barrier response in a parametric study are investigated.
36 The results from this study provide useful guidance for future design and optimization of rockfall
37 barriers in engineering practice.

38
39
40
41
42 **Keywords:**

- 43 Rockfall hazard
- 44 Flexible ring net barrier
- 45 Discrete element method
- 46 Physical model impact test
- 47 Rockfall-barrier interaction

1
2
3
4
5
6
7
8
9
10
11
12
13
14
15
16
17
18
19
20
21
22
23
24
25
26
27
28
29
30
31
32
33
34
35
36
37
38
39
40
41
42
43
44
45
46
47
48
49
50
51
52
53
54
55
56
57
58
59
60
61
62
63
64
65

46 **1. Introduction**

47 Rockfall hazard is significant rapid movement of detached rock fragments with different
48 volumes by freefalling, bouncing, rolling and sliding over long distances in mountainous areas
49 [1]. It poses a great threat to people’s lives and infrastructures due to its sudden and destructive
50 power. Thus, adequate protective countermeasures are required to be designed and applied to
51 risk mitigation. Over the last few years, flexible barriers, as one of the effective retention systems
52 among mitigation measures, have been extensively used in Europe to intercept high-energy
53 falling rocks. They have perfect bearing capacity to sustain dynamic loading of rockfalls owing
54 to their high ductility and excellent energy dissipation performance.

55 With the aim of gaining better understanding of the dynamic behavior of the flexible barrier
56 system and rockfall-barrier interaction mechanisms, field tests and experimental programs were
57 carried out in the past few decades [2-9]. Generally, the test was composed of a barrier prototype
58 against the impact of a boulder with known mass released from a certain height at an inclined
59 site [2,4] or a vertical site [5,7]. Various monitoring techniques were employed to meet the
60 requirements of all measurements. The boulder motion and barrier response were tracked by
61 high-speed cameras. The loadings on barrier were recorded by means of multiple load cells
62 installed on cables and posts. However, as the key component of the barrier system, the tensile
63 forces developed on interception structure have rarely been concerned due to the difficulty of
64 load cells installation, particularly for the circular ring net. Therefore, an improved monitoring
65 approach for rockfall impact test is in demand to collect reliable data on barrier directly.

66 Nevertheless, to consider all the loading cases and geometrical configurations in physical
67 modeling tests is unrealistic and expensive in terms of time and money. Alternatively, the

1
2
3
4 68 numerical approaches have become a powerful and efficient tool to study the dynamic response
5
6 69 of flexible barriers. Either finite element (FE) [10-16] or discrete element (DE) [17] strategies
7
8
9 70 were developed in the literature. Compared with the finite element method (FEM), the discrete
10
11 71 element method (DEM) has the advantage of describing large displacements and failure mode at
12
13
14 72 element scale for flexible barrier modeling. Meanwhile, rockfall-barrier interaction can be easily
15
16 73 simulated attributed to its inherent merit in describing granular media. With the DEM, barrier
17
18
19 74 models were mainly established on the basis of either remote interaction model [18] or cylinder
20
21 75 model [19] considering different shapes of the net including hexagonal mesh [18,20,21], pear-
22
23
24 76 shaped mesh [22] and 45° rotated square mesh [23]. However, only limited studies [24,25] on
25
26 77 ring net mesh with the DEM has been reported due to its complex structure and special
27
28
29 78 mechanical response. The parameters in the simulation are highly rely on accurate and reliable
30
31 79 data from experimental calibration tests. There is lack of a systematic calibration process on
32
33
34 80 various components of a flexible ring net barrier. A thorough validation based on large-scale
35
36 81 physical model test is still unavoidable. Besides, it is of essential significance to deeply analyze
37
38
39 82 the factors that affect the impact behavior of a flexible ring net barrier.
40

41
42 83 This article presents a newly developed flexible ring net barrier model based on the DEM to
43
44 84 simulate the rockfall impact on a flexible barrier. A systematic calibration approach is elaborated
45
46 85 in detail. The capabilities of the numerical model are evaluated by comparing the results from
47
48
49 86 novel designed large-scale physical model impact tests. In addition, the effects of boulder size,
50
51 87 impact position, barrier inclination and barrier initial slack on barrier response are investigated.
52
53
54 88 The results provide useful guidance for future design and optimization of rockfall barriers in
55
56 89 engineering practice.
57
58
59
60 90

91 **2. Large-scale physical model impact tests**

92 The large-scale physical model testing facility, built at the Road Research Laboratory of The
93 Hong Kong Polytechnic University, was specially designed by the authors to study the rockfall-
94 barrier impact mechanisms. The tests pave the way for the calibration, evaluation and parametric
95 study of the numerical model.

96 *2.1. Experimental setup and instrumentation*

97 The main body of the steel frame physical model is formed by three parts: a 5 m³ container
98 with a mechanical gate-release device, a 7 m long and 1.5 m wide flume with tempered glass on
99 both sides for real-time observation, and a flexible barrier system as displayed in Fig. 1a. Fig. 1b
100 shows a schematic side view of the physical model. The channel inclination is 35° and it is
101 perpendicular to the barrier system. Fig. 2a illustrates the front view of the barrier system. 28
102 high-grade steel wire rings and a steel wire rope constituted the net with dimensions of 2.48 m ×
103 1.48 m. The 300 mm diameter ring element was obtained by twisting seven times the same 3 mm
104 diameter steel wire. Each individual ring element connected with other four neighboring
105 elements within the net. The rope was linked to the rigid steel posts via shackles at the four top
106 corners. Besides, to directly measure the impact force on the barrier, ten original designed
107 tension link transducers (No.1-10) with a capacity of 20 kN (Fig. 2c) were mounted on the
108 predicted impact central area of the net. Fig. 2b gives a schematic diagram of the locations of the
109 transducers. Two high-speed cameras synchronized with the transducers, one at the front, one at
110 the side of the flexible barrier, tracked the boulder motion and net response employing a
111 resolution of 1024 × 768 pixels and a frame rate of 1000 f/s.

112 *2.2. Testing procedures*

1
2
3
4
5
6
7
8
9
10
11
12
13
14
15
16
17
18
19
20
21
22
23
24
25
26
27
28
29
30
31
32
33
34
35
36
37
38
39
40
41
42
43
44
45
46
47
48
49
50
51
52
53
54
55
56
57
58
59
60
61
62
63
64
65

113 A granite spherical boulder with a density of 2650 kg/m^3 was lifted into the container from
114 ground level with the help of the electric chain hoist. The boulder was released by triggering the
115 gate-release device through a novel designed pulley system. Two launches with two distinct
116 boulder diameters (400 mm and 600 mm) were performed.

118 **3. Numerical modeling with the DEM and model calibration**

119 In this section, a numerical model of the flexible ring net barrier system based on the DEM is
120 developed. The Edinburgh Bonded Particle Model (EBPM) originally proposed for modeling
121 cementitious materials [26] was adopted for describing different components of the barrier
122 system. Each component was idealized as an assembly of spherical particles connected by virtual
123 beam-like bond elements. The behavior of the bond element is governed by the Timoshenko
124 beam theory, which provides a realistic mechanics-based representation of the interaction
125 between particles, in contrast to some of the remote interaction models such as the Hertz-Mindlin
126 with bonding model [27]. All the input mechanical parameters were calibrated by means of
127 laboratory tests. EDEM [28] is used as the tool to perform the simulations.

128 *3.1. Ring net element*

129 The circular ring net element is modeled by bonding a certain number of same-sized
130 spherical particles together to form a closed loop employing the EBPM, as shown in Fig. 3a. Fig.
131 3b schematically describes bond formation between any two adjacent particles. Each particle has
132 its own physical radius and contact radius. Only a contact radius overlap exists between two
133 particles that are not in physical contact can they be bonded together once the bond time is
134 reached. The bond element rigidly links two particles via the centres of spheres. Fig. 3c gives the

1
2
3
4 135 6 forces and 6 moments acting on both ends of a cylindrical beam element, which will be
5
6
7 136 updated incrementally at every time step. The resulting forces can be expressed as:

$$10 \quad \mathbf{F} = \mathbf{K} \cdot \mathbf{u} \quad (1)$$

11
12
13 138 where $\mathbf{F} = [F_{ix} \quad F_{iy} \quad F_{iz} \quad M_{ix} \quad M_{iy} \quad M_{iz} \quad F_{jx} \quad F_{jy} \quad F_{jz} \quad M_{jx} \quad M_{jy} \quad M_{jz}]^T$;

14
15
16
17 139 $\mathbf{u} = [s_{ix} \quad s_{iy} \quad s_{iz} \quad \theta_{ix} \quad \theta_{iy} \quad \theta_{iz} \quad s_{jx} \quad s_{jy} \quad s_{jz} \quad \theta_{jx} \quad \theta_{jy} \quad \theta_{jz}]^T$. \mathbf{F} contains axial forces, shear

18
19
20 140 forces, twisting moments and bending moments. \mathbf{u} is the corresponding displacement vector

21
22 141 where s and θ donate the displacements and rotations. \mathbf{K} is a tangential stiffness matrix

23
24 142 derived from the Timoshenko beam theory. The bond element will be broken if the maximum

25
26
27 143 bond stress exceeds either tensile strength σ_T or shear strength τ expressed as follows:

$$28 \quad \sigma_T \leq \frac{F_{\delta x}}{A_b} + \frac{r_b \sqrt{M_{\delta y}^2 + M_{\delta z}^2}}{I_b} \quad \delta = i, j \quad (2)$$

$$29 \quad \tau \leq \frac{M_{\delta x} r_b}{2I_b} + \frac{4\sqrt{F_{\delta y}^2 + F_{\delta z}^2}}{3A_b} \quad \delta = i, j \quad (3)$$

30
31
32 144 where r_b , A_b and I_b are the disc radius, cross-sectional area and moment of inertia of the bond

33
34
35
36
37 145 ($A_b = \pi r_b^2$; $I_b = \frac{\pi r_b^4}{4}$). It should be noted that the bond exhibits a linear elastic response. By

38
39
40
41 146 making using of the natural advantage of the DEM in dealing with geometric nonlinear problem,

42
43
44 147 the ring behavior with large stretching deformation in both static and dynamic conditions can be

45
46
47 148 easily replicated through carefully calibration on the stiffness and strength of a ring net element.

48
49
50
51 149 Quasi-static tensile tests of single wire rings and groups of wire rings were performed in the

52
53
54 150 Swiss federal Institute of Technology Zurich ETHZ [5], which were utilized for ring net element

1
2
3
4 153 calibration. The tested rings were fixed to a steel double plates apparatus on both upper and
5
6
7 154 lower sides as presented in Fig. 4a. A constant loading velocity (0.2mm/s) was applied to the top
8
9 155 double plates. Fig. 5a records the load-displacement relationship for a single wire ring. Two
10
11 156 domains can be identified from ring's shape evolution: bending domain and tensile domain [25].
12
13
14 157 In bending domain, the ring deforms significantly, and the tensile force increases slowly. In
15
16 158 tensile domain, the deflections are small, and the tensile force grows considerably until the ring
17
18
19 159 breaks. The two domains provide insights on how the bending and tensile stiffness dominate the
20
21 160 ring's response in different stages. In order to reproduce the same response of the ring net
22
23
24 161 element in the DE model, the identical test setup was established as demonstrated in Fig. 4b.
25
26 162 There are three main mechanical parameters need to be calibrated: bond radius (r_b), bond
27
28
29 163 Young's modulus (E_b) and bond tensile strength (σ_T), where r_b and E_b exert direct influence on
30
31
32 164 the rigidity of a ring element and σ_T determines its breaking force. The ring net element is
33
34
35 165 modeled as a single wire with an equivalent cross-sectional area A_{eq} defined as

$$A_{eq} = \pi r_{eq}^2 = \pi r_w^2 n_w \quad (4)$$

36
37
38
39 166 where r_{eq} is the equivalent particle radius; r_w is the wire radius; n_w is the number of turns.
40
41
42 167 However, it is worth noting that considering such an equivalent cross section overestimates the
43
44
45 168 bending stiffness due to the enlarged moment of inertia [14]. In the meantime, the axial stiffness
46
47
48 169 is only one-fifth of the theoretical value due to the different utilization of the individual wires [5].
49
50
51 170 Therefore, two reduction factors p and q related to E and r_{eq} (steel Young's modulus)
52
53
54 171 respectively are assumed to calibrate the axial (K_a) and bending stiffness (K_b) separately:
55
56
57
58

$$K_a = 0.2E\pi r_w^2 n_w = E_b \pi r_b^2 = pq^2 E \pi r_{eq}^2 \quad (5)$$

$$K_b = E_b \pi \frac{r_b^4}{4} = pq^4 E \pi \frac{r_{eq}^4}{4} \quad (6)$$

where $E_b = pE$, $r_b = qr_{eq}$. Finally, a good calibration results were obtained when $r_b = 2 \text{ mm}$, $E_b = 160 \text{ GPa}$ and $\sigma_T = 21 \text{ GPa}$, matching the response in both bending and tensile domains at the ring and mesh scale (Fig. 5).

3.2. Steel strand cable

A filler wire with nominal diameter of 20 mm which construction has small auxiliary wires for spacing and positioning other wires was used as the steel wire rope in the physical model tests. To characterize the mechanical behavior of the cable and calibrate the DE model, quasi-static tensile tests were performed on the Universal Testing machine in The Hong Kong Polytechnic University (Fig. 6a). The tested specimens with lengths of 60 cm were restrained by the specially designed clamps at the two ends to avoid slippage on wires. An extensometer with a gauge length of 100 mm was installed in the middle of the specimens for strain measurement. The tests were conducted in displacement control with a loading velocity of 6 mm/min. For safety and device protection purposes, the tensile tests were stopped at almost 70% of the theoretical breaking strength (265 kN), and thus the elastic modulus (138 GPa) was collected from the linear behavior of the strand cable. Fig. 6b plots the axial stress of the specimen varying with the axial strain.

3.3. Shackles

There were 18 Screw Pin Anchor Shackles with a Working Load Limit (WLL) of 2 tons used for connecting the ring net and steel strand cable in the barrier system. The deformation of these shackles during the impact tests is ignored because the estimated maximum tensile force between

1
2
3
4 195 ring net elements is much less than the shackles Ultimate Strength. Hence the shackle is
5
6 196 described as a 6 cm × 8 cm rectangular hoop with much higher stiffness than the ring net
7
8
9 197 element and strand cable in the DE model. Each shackle is bonded by 14 particles and can slide
10
11
12 198 along with the cable and connected rings. Fig. 7a depicts the detail arrangement of different
13
14 199 components of the flexible ring net barrier at particle generation stage of the DE model.

17 200 *3.4. Model setup*

20 201 Fig. 7b demonstrates the full-scale numerical model setup. A spherical boulder particle is
22
23 202 placed in the steel container before being released to the slope channel. The channel boundaries
24
25 203 consist of a rigid steel baseplate and two fixed side walls. The flexible ring net barrier system is
26
27
28 204 established by the same number and arrangement of the ring net elements, steel strand cable and
29
30 205 shackles with the physical model. All the bonded particles are generated by the EDEM
31
32
33 206 Application Programming Interface (API). The steel wire cable is assumed to be linked with four
34
35 207 rigid steel rings allowing rotation and sliding at the four corners to simulate the connected
36
37
38 208 shackles at the rigid steel posts. It is worth noting that a flexible ring net would produce an initial
39
40 209 slack induced by the gravity and overlaps between ring net elements as shown in Fig. 7b. The
41
42
43 210 initial slack (ψ) is defined as:

$$44
45
46
47 211 \psi = \frac{h}{d} \quad (7)$$

48
49
50
51 212 where h represents the height difference between the two overlapped ring elements in the
52
53 213 vertical direction. d is the diameter of a ring net element (300 mm). In order to accurately
54
55
56 214 replicate the same initial slack as the experiment in the DE model, different attempts on the
57
58
59
60
61
62
63
64
65

1
2
3
4
5
6
7
8
9
10
11
12
13
14
15
16
17
18
19
20
21
22
23
24
25
26
27
28
29
30
31
32
33
34
35
36
37
38
39
40
41
42
43
44
45
46
47
48
49
50
51
52
53
54
55
56
57
58
59
60
61
62
63
64
65

215 values of initial slack were made under the gravitational acceleration to obtain a similar initial
216 state of the barrier with the test.

217

218 **4. Model evaluation**

219 To evaluate the effectiveness and overall performance of the DE model, comparison with the
220 experimental results is examined in terms of boulder velocities, net elongations and tensile forces
221 developed between ring net elements in this section.

222 *4.1. Boulder velocities and net elongations*

223 Fig. 8 compares the experimental and numerical dynamic response of the flexible ring net
224 barrier of the two rockfall impact tests. Three time points that demonstrate the different impact
225 moments are selected for comparison: (a) The boulder contacts with the net for the first time; (b)
226 The boulder velocity decreases rapidly due to the increased elastic deformation of the ring net
227 barrier. (c) The boulder velocity reduces to zero and the maximum net elongation is achieved.
228 Only elastic deformation is observed for both tests. The time evolution of the boulder velocity
229 and net elongation for the two tests is depicted in Fig. 9. Time 0 corresponds to the first contact
230 of the boulder with the barrier. It is found that the interaction between the boulder and barrier is
231 accurately reproduced with the DE model. The impact area and deformed shape of the barrier are
232 consistent with the experiments. The trajectory of the boulder in the model agrees well with that
233 in the experiment. Notably, at the third time points, the maximum net elongation is reached when
234 the boulder is moving upward due to the vertical component of the net tension force, matching
235 the boulder-barrier interaction in the experiments. Besides, it is observed that the maximum
236 elongation of the barrier in the simulation is slightly less than that in the experiment in both tests.

1
2
3
4
5
6
7
8
9
10
11
12
13
14
15
16
17
18
19
20
21
22
23
24
25
26
27
28
29
30
31
32
33
34
35
36
37
38
39
40
41
42
43
44
45
46
47
48
49
50
51
52
53
54
55
56
57
58
59
60
61
62
63
64
65

237 The reason for this difference is because the installed steel strand cable in the tests is relatively
238 loose that may cause additional elongation during the impact, whereas this effect cannot be taken
239 into account in the DE model although initial slack of the ring net has already been considered.

240 *4.2. Tensile forces developed between ring net elements*

241 The ring net plays a major role in energy absorption and force transmission during the impact
242 process. However, the tensile forces developed on ring net are rarely measured in the literature.
243 In our experiment, the values of tensile forces were recorded by ten tension link transducers (see
244 sensors number in Fig. 2) installed on the predicted impact central area of the net. In the DE
245 model, the forces at the identical locations are obtained by detecting the normal contact forces
246 between ring net elements. Fig. 10 and Fig. 11 depict the experimental and numerical time
247 histories of the tensile forces at various positions of impact area for the two tests. Time 0
248 corresponds to the barrier starting to deform. Half of the transducers are selected at the same
249 height in each test for comparison (transducers No.2, 4, 6, 8, 10 for test 1; transducers No.1, 3, 5,
250 7, 9 for test 2) due to the symmetry of their locations. The DE model accurately captures the
251 general trend of the tensile forces with time including all the peak values. The maximum tensile
252 forces appear at the positions of transducer 10 (7.86 kN) and transducer 3 (28.05 kN) in test 1
253 and test 2 respectively, which is in good agreement with the experimental observations. The
254 reasons for different positions of the maximum tensile forces occurred in the two tests should be
255 explained in two aspects. First, different boulder sizes may lead to different sizes of contact
256 surface on net. Second, different travel distances and lifting heights of the boulders caused
257 different locations of the contact surface on net. In addition, the peak values not always take
258 place exactly at the same time in the simulation as well as in the experimental study.

1
2
3
4
5
6
7
8
9
10
11
12
13
14
15
16
17
18
19
20
21
22
23
24
25
26
27
28
29
30
31
32
33
34
35
36
37
38
39
40
41
42
43
44
45
46
47
48
49
50
51
52
53
54
55
56
57
58
59
60
61
62
63
64
65

259

260 **5. Parametric analysis**

261 In the previous section, it is proved that the DE model provides satisfactory estimations of
262 the barrier dynamic response under the boulder impact. Thus, further parametric studies related
263 to the impact behavior can proceed to serve for the design. As the key index for flexible barrier
264 design, the impact force is influenced by many factors. In this section, the effects of the factors
265 on the impact force are investigated from a series of parametric analysis.

266 *5.1. Effect of the boulder size*

267 Four different boulder diameters (D) are examined for impact force comparison: 400 mm,
268 500 mm, 600 mm and 700 mm (Fig. 12). Time 0 refers to the first contact of the boulder with the
269 barrier. As the boulder size increases, the impact force rises significantly fast until reaching the
270 peak value. The peak impact force of the boulder with 700 mm in diameter is 110.96 kN, almost
271 6 times than the boulder with 400 mm in diameter (20.09 kN). Besides, with the same velocities
272 at the slope base before impact for different boulder sizes, small boulder can move longer
273 distance than large boulder as observed in Fig. 9. Therefore, the time taken for reaching the peak
274 impact force is negative correlated with the boulder size. From a practical point of view, if we
275 can estimate the sizes of the potential falling rocks in a specific region, the maximum impact
276 force can be easily calculated by numerical simulations, and thus it is possible to optimize the
277 barrier design in various areas.

278 *5.2. Effect of the impact location*

1
2
3
4
5
6
7
8
9
10
11
12
13
14
15
16
17
18
19
20
21
22
23
24
25
26
27
28
29
30
31
32
33
34
35
36
37
38
39
40
41
42
43
44
45
46
47
48
49
50
51
52
53
54
55
56
57
58
59
60
61
62
63
64
65

279 In the experiment, the boulder was released from the bottom centre of the container, and thus
280 the impact occurred at the central area of the ring net. However, a falling rock can hit to any
281 locations of the net. Hence, the effects of five different impact locations (from -0.36 m to 0.36 m)
282 on the peak impact forces are examined. Fig. 13 demonstrates both the peak impact force and
283 maximum elongation evolution with impact location. The x-axis represents horizontal locations
284 of the net. Compared with in the middle of the barrier, relatively small number of rings are able
285 to participate in energy dissipation including deflections and sliding motions when the impact
286 area is close to the edge of the barrier. As a result, the average peak impact force near the edge of
287 the barrier is larger than that in the middle. While the opposite trend is observed for the average
288 maximum elongation of the barrier. In the design of the ring net, it is necessary to evaluate the
289 peak impact forces and maximum elongations considering different impact locations and find out
290 the weakest point of the net to optimize the design.

291 *5.3. Effect of the angle between the barrier and slope*

292 The barrier positions varied in past studies, either parallel to the gravity vector [23] or normal
293 to the slope [18,21]. However, this factor can indeed influence the impact force on barrier. Three
294 tested angles (α) vary from 55° (parallel to the gravity vector) to 90° (normal to the slope). Fig.
295 14 plots the time histories of the impact force on barrier for three different angles. It is found that
296 the impact process occurs earlier with the decreased angle. Due to the larger stretching force in
297 the vertical direction, the interaction time gets reduced, and thus larger peak impact force is
298 observed. The peak impact force for 55° (92.55 kN) is 26.74% larger than 90° (73.02 kN). This
299 study highlights that in order to get smaller impact force, the barrier is suggested to be
300 perpendicular to the slope. Alternatively, a buffer zone shall be set in front of the slope base
301 before build a barrier.

302 *5.4. Effect of the initial slack of a ring net barrier*

303 Based on Eq. (7), five different initial slack values of the ring net are considered. The same
304 boulder size (600 mm) is used for all cases. Fig. 15 displays the correlation of the peak impact
305 force with the initial slack of a ring net barrier. For a small initial slack (0.35), the average value
306 of peak impact forces remains at a relatively higher level (71.43 kN). With the initial slack
307 increased to 0.4, it shows a negative correlation between the peak impact force and the initial
308 slack. The average value of peak impact forces falls by 8.15%. This effect is attributed to the
309 reduced overall stiffness of the flexible barrier, leading to smaller impact forces to absorb the
310 same amount of energy. However, with the slack further goes up, the kinetic energy of the
311 boulder also increases owing to longer moving distances. The decreased overall stiffness of the
312 net is insufficient to balance the increased kinetic energy, leading to larger impact forces, and
313 thus the peak impact force is positive correlated with the initial slack when it is larger than 0.4.
314 Therefore, the simulation results indicate that the initial slack could be an important factor that
315 may affect the peak impact force acting on a flexible ring net barrier. It is necessary to figure out
316 a safety range for the initial slack in barrier design. Further experimental studies are
317 recommended to be carried out.

319 **6. Conclusions**

320 In this paper, a new flexible ring net barrier model is developed based on the discrete element
321 method. The Edinburgh Bonded Particle Model was adopted for describing different components
322 of the barrier system. All the input mechanical parameters were calibrated by means of
323 laboratory tests. Large-scale rockfall impact tests were conducted to study the rockfall-barrier

1
2
3
4
5
6
7
8
9
10
11
12
13
14
15
16
17
18
19
20
21
22
23
24
25
26
27
28
29
30
31
32
33
34
35
36
37
38
39
40
41
42
43
44
45
46
47
48
49
50
51
52
53
54
55
56
57
58
59
60
61
62
63
64
65

324 interaction. The effectiveness and overall performance of the discrete element model are
325 evaluated by comparison with the experimental results. Finally, the effects of the factors on the
326 impact force are investigated by a series of parametric analysis. Based on these works, the main
327 findings are drawn as follows:

- 328 1. The calibration of mechanical parameters in different components of the barrier system can be
329 easily done by means of laboratory tests.
- 330 2. The new DE model is able to reproduce the behavior of a ring net barrier under rockfall
331 impact. A good agreement with experimental data can be found regarding to boulder
332 velocities, net elongations and tensile forces developed between ring net elements.
- 333 3. To optimize a barrier design, it is necessary to evaluate the peak impact forces considering
334 different boulder sizes and impact locations.
- 335 4. The barrier is suggested to be perpendicular to the slope to get smaller impact force.
336 Alternatively, a buffer zone shall be set in front of the slope base before build a barrier.
- 337 5. The initial slack of a flexible barrier is an important factor that may affect the peak impact
338 force acting on net. It is necessary to figure out a safety range for the initial slack in barrier
339 design.
- 340 6. The new DE model has a great potential for studying the interaction mechanisms between
341 granular flows and flexible barriers owing to the inherent merits of the DEM. More
342 complicated parametric studies are allowed to carry out. Large-scale physical model impact
343 tests related to granular flows are recommended to be conducted to further validate the
344 proposed new numerical model.

1
2
3
4
5
6
7
8
9
10
11
12
13
14
15
16
17
18
19
20
21
22
23
24
25
26
27
28
29
30
31
32
33
34
35
36
37
38
39
40
41
42
43
44
45
46
47
48
49
50
51
52
53
54
55
56
57
58
59
60
61
62
63
64
65

345

Acknowledgements

346

347

The authors would like to thank Professor Jin Ooi from the University of Edinburgh for providing the source code of the Bonded Particle Model on updating and Professor Jian-Fei Chen of Queen’s University Belfast for advising us on the bond modeling and DEM modeling. The authors acknowledge the financial support from Research Institute for Sustainable Urban Development of The Hong Kong Polytechnic University (PolyU) and Research Centre for Urban Hazards Mitigation of Faculty of Construction and Environment of PolyU. The work in this paper is also supported by a CRF project (Grant No.: PolyU12/CRF/13E) from Research Grants Council (RGC) of Hong Kong Special Administrative Region Government of China. The financial supports from PolyU grants (1-ZVCR, 1-ZVEH, 4-BCAU, 4-BCAW, 4-BCB1, 5-ZDAF) are acknowledged.

357

1
2
3
4 **358 References**

- 5
6
7
8 359 [1] Cruden DM, Varnes DJ. Chapter 3: Landslides types and processes. In: Turner AK, Schuster
9
10 360 RL, eds. Landslides: Investigation and Mitigation. Washington DC: Transportation Research
11
12 361 Board, National Academy of Sciences; 1996:36-75.
- 13
14
15
16 362 [2] Smith DD, Duffy JD. Field tests and evaluation of rockfall restraining nets. Report No.
17
18 363 CA/TL-90/05, California Department of Transportation, San Luis Obispo, California; 1990.
- 19
20
21 364 [3] Hearn G, Barret RK, Henson HH. Testing and modelling of two rockfall barriers.
22
23 365 Transportation research record 1504. Washington DC: National Academic Press; 1995.
- 24
25
26 366 [4] Peila D, Pelizza S, Sassudelli F. Evaluation of behaviour of rockfall restraining nets by full
27
28 367 scale tests. Rock Mechanics and Rock Engineering 1998;31(1):1-24.
- 29
30
31
32 368 [5] Grassl HG. Experimentelle und numerische Modellierung des dynamischen Trag-und
33
34 369 Verformungsverhaltens von hochflexiblen Schutzsystemen gegen Steinschlag PhD. thesis
35
36 370 Switzerland: ETH Zurich; 2002.
- 37
38
39
40 371 [6] Arndt B, Ortiz T, Turner A. Colorado's full-scale field testing of rockfall attenuator systems.
41
42 372 Transportation research circular, E-C141. Washington DC: Transportation Research Board,
43
44 373 National Academy of Sciences; 2009:130.
- 45
46
47
48 374 [7] Gottardi G, Govoni L. Full-scale modelling of falling rock protection barriers. Rock
49
50 375 Mechanics and Rock Engineering 2010;43(3):261-274.
- 51
52
53
54 376 [8] Buzzi O, Spadari M, Giacomini A, Fityus S, Sloan SW. Experimental testing of rockfall
55
56 377 barriers designed for the low range of impact energy. Rock Mechanics and Rock Engineering
57
58 378 2013;46(4):701-712.
- 59
60
61
62
63
64
65

1
2
3
4
5
6
7
8
9
10
11
12
13
14
15
16
17
18
19
20
21
22
23
24
25
26
27
28
29
30
31
32
33
34
35
36
37
38
39
40
41
42
43
44
45
46
47
48
49
50
51
52
53
54
55
56
57
58
59
60
61
62
63
64
65

[9] Gao Z, Al-Budairi H, Steel A. Experimental testing of low-energy rockfall catch fence meshes. *Journal of Rock Mechanics and Geotechnical Engineering* 2018;10(4):798-804.

[10] Cazzani A, Mongiovi L, Frenez T. Dynamic finite element analysis of interceptive devices for falling rocks. *International Journal of Rock Mechanics and Mining Sciences* 2002;39(3):303-321.

[11] Gentilini C, Govoni L, Miranda SD, Gottardi G, Ubertini F. Three-dimensional numerical modelling of falling rock protection barriers. *Computers and Geotechnics* 2012;44:58-72.

[12] Gentilini C, Gottardi G, Govoni L, Mentani A, Ubertini F. Design of falling rock protection barriers using numerical models. *Engineering Structures* 2013;50:96-106.

[13] Volkwein A. Numerische simulation von flexiblen steinschlagschutzsystemen PhD. thesis Switzerland: ETH Zurich; 2004.

[14] Escallón JP, Wendeler C. Numerical simulations of quasi-static and rockfall impact tests of ultra-high strength steel wire-ring nets using Abaqus/Explicit. In: 2013 SIMULIA Community conference; 2013.

[15] Escallón J, Boetticher V, Wendeler C, Chatzi E, Bartelt P. Mechanics of chain-link wire nets with loose connections. *Engineering Structures* 2015;101:68-87.

[16] Mentani A, Giacomini A, Buzzi O, Govoni L, Gottardi G, Fityus S. Numerical modelling of a low-energy rockfall barrier: new insight into the bullet effect. *Rock Mechanics and Rock Engineering* 2016;49(4):1247-1262.

[17] Cundall PA, Strack ODL. A discrete numerical model for granular assemblies. *Géotechnique* 1979;29(1):47- 65.

1
2
3
4
5
6
7
8
9
10
11
12
13
14
15
16
17
18
19
20
21
22
23
24
25
26
27
28
29
30
31
32
33
34
35
36
37
38
39
40
41
42
43
44
45
46
47
48
49
50
51
52
53
54
55
56
57
58
59
60
61
62
63
64
65

[18] Bertrand D, Nicot F, Gotteland P, Lambert S. Discrete element method (DEM) numerical modeling of double-twisted hexagonal mesh. Canadian Geotechnical Journal 2008;45(8):1104-1117.

[19] Bourrier F, Kneib F, Chareyre B, Fourcaud T. Discrete modeling of granular soils reinforcement by plant roots. Ecological Engineering 2013;61:646-657.

[20] Thoeni K, Lambert C, Giacomini A, Sloan SW. Discrete modelling of hexagonal wire meshes with a stochastically distorted contact model. Computers and Geotechnics 2013;49:158-169.

[21] Li X, Zhao J. A unified CFD-DEM approach for modeling of debris flow impacts on flexible barriers. International Journal for Numerical and Analytical Methods in Geomechanics 2018;42(14):1643-1670.

[22] Bertrand D, Trad A, Limam A, Silvani C. Full-scale dynamic analysis of an innovative rockfall fence under impact using the discrete element method: from the local scale to the structure scale. Rock Mechanics and Rock Engineering 2012;45(5):885-900.

[23] Albaba A, Lambert S, Kneib F, Chareyre B, Nicot F. DEM modeling of a flexible barrier impacted by a dry granular flow. Rock Mechanics and Rock Engineering 2017;50(11):3029-3048.

[24] Nicot F, Cambou B, Mazzoleni G. From a constitutive modelling of metallic rings to the design of rockfall restraining nets. International Journal for Numerical and Analytical Methods in Geomechanics 2001;25(1):49-70.

[25] Coulibaly JB, Chanut M-A, Lambert S, Nicot F. Nonlinear discrete mechanical model of

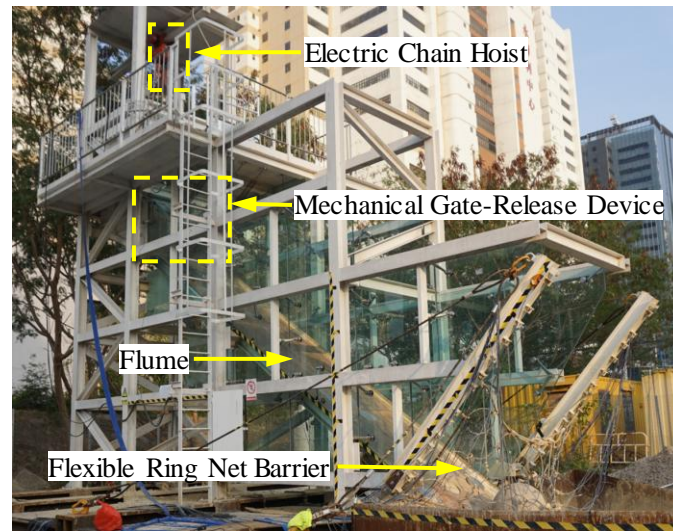
1
2
3
4
5
6
7
8
9
10
11
12
13
14
15
16
17
18
19
20
21
22
23
24
25
26
27
28
29
30
31
32
33
34
35
36
37
38
39
40
41
42
43
44
45
46
47
48
49
50
51
52
53
54
55
56
57
58
59
60
61
62
63
64
65

421 steel rings. Journal of Engineering Mechanics 2017;143(9):04017087.

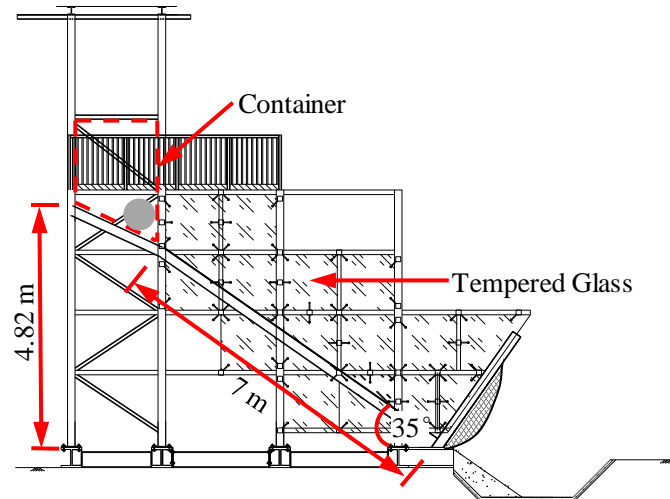
422 [26] Brown NJ, Chen J-F, Ooi, JY. A bond model for DEM simulation of cementitious materials
423 and deformable structures. Granular Matter 2014;16(3):299-311.

424 [27] DEM Solutions: EDEM 2.6 Theory Reference Guide. Edinburgh, UK; 2014.

425 [28] DEM Solutions: EDEM 2017. Edinburgh, UK; 2016.

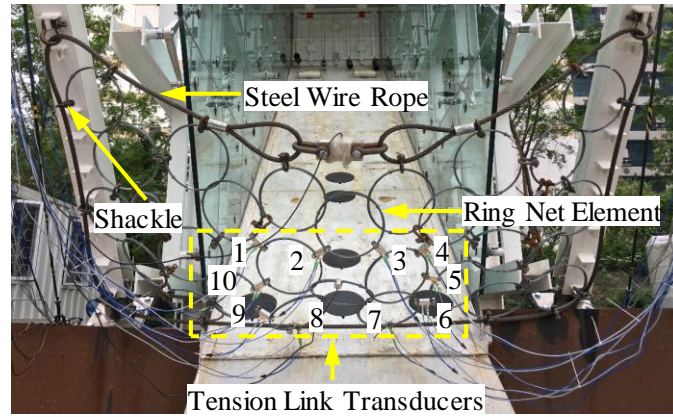


(a)

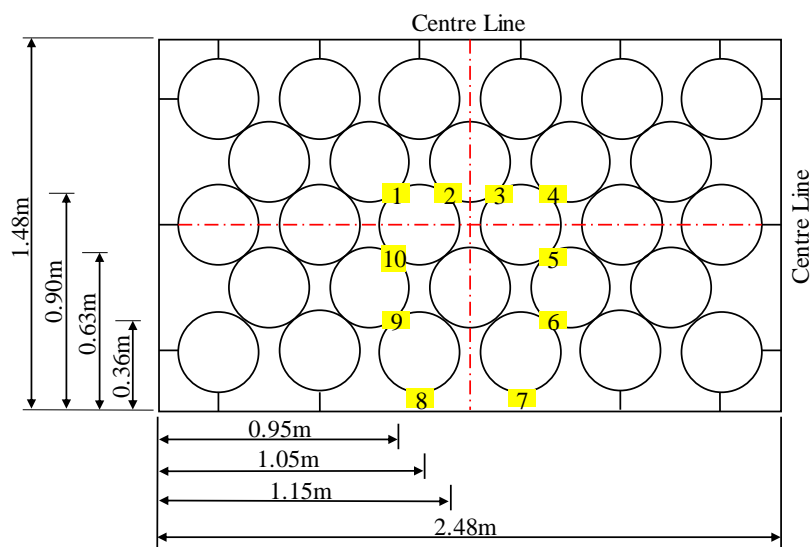


(b)

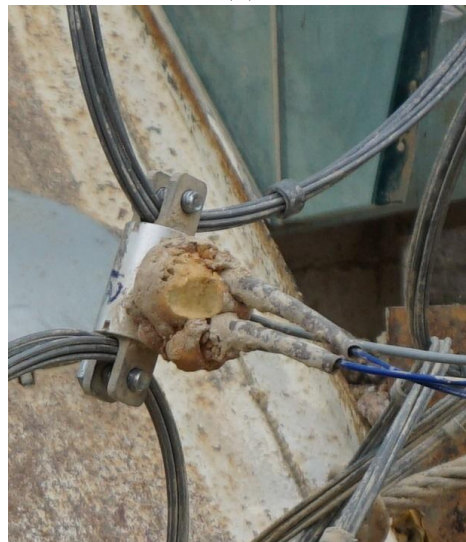
Fig. 1. The large-scale physical model testing facility: (a) panoramic view (b) side view.



(a)



(b)



(c)

Fig. 2. The flexible barrier system: (a) front view (b) schematic diagram of the locations of the transducers (c) a tension link transducer.

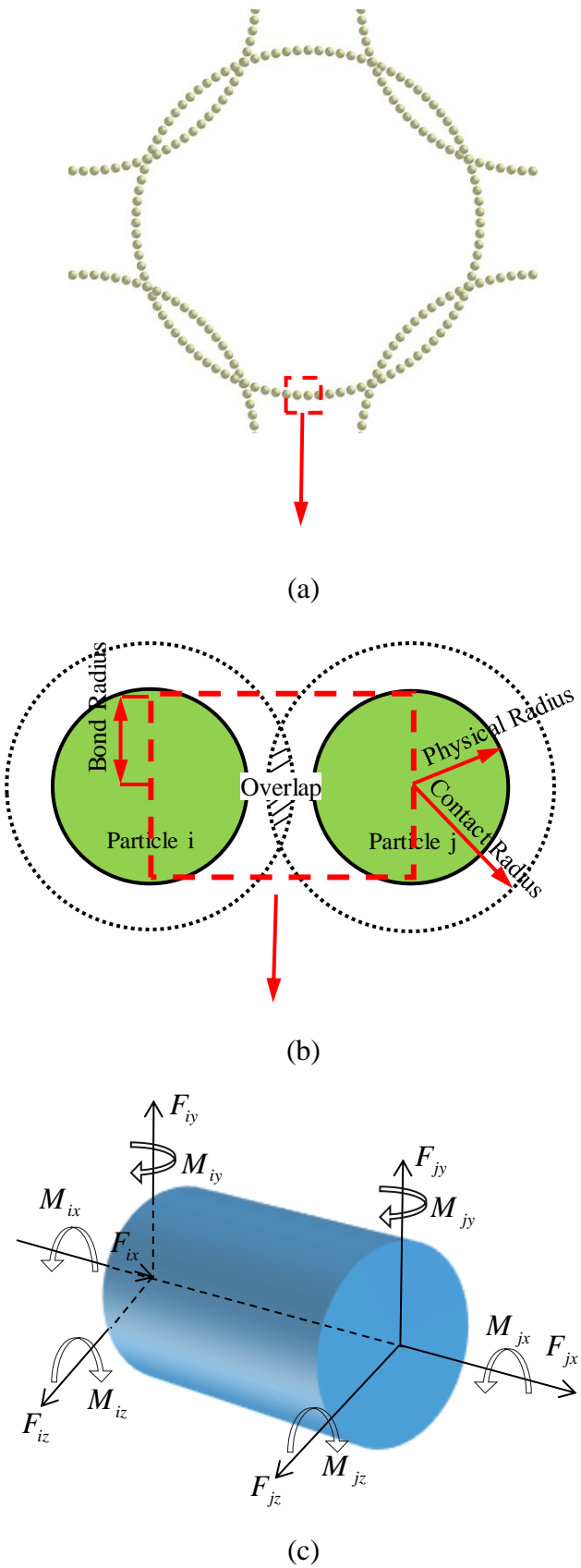


Fig. 3. Bond formation with the EBPM between particles: (a) a ring net element (b) a sample of two bonded particles by a Timoshenko beam element (c) forces and moments acting on a bond element.

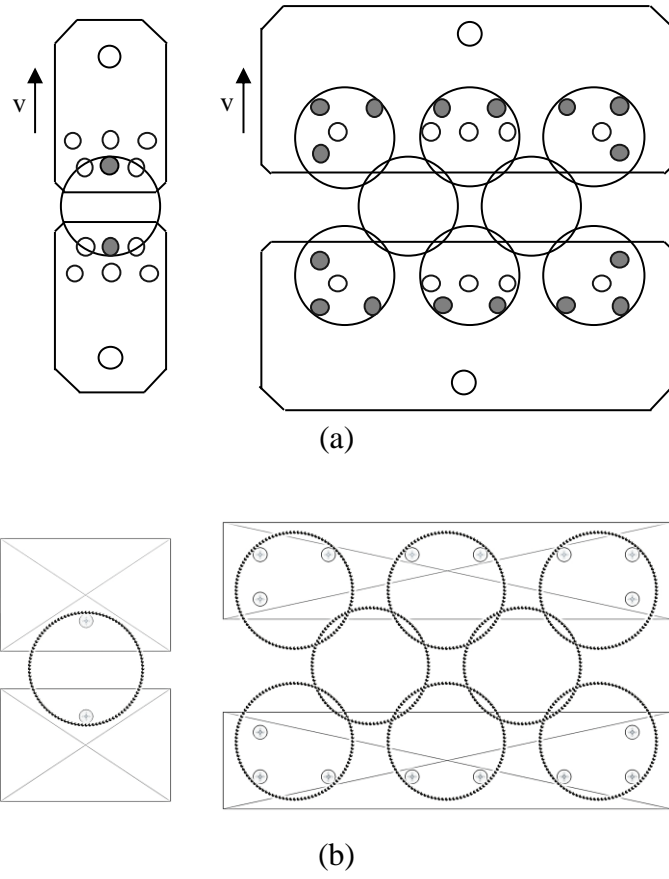
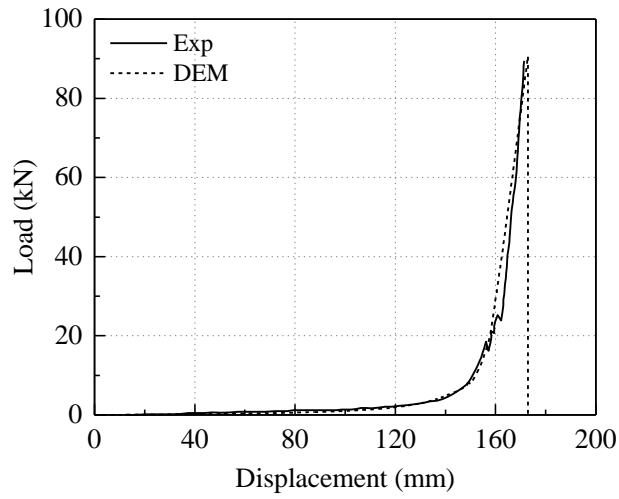
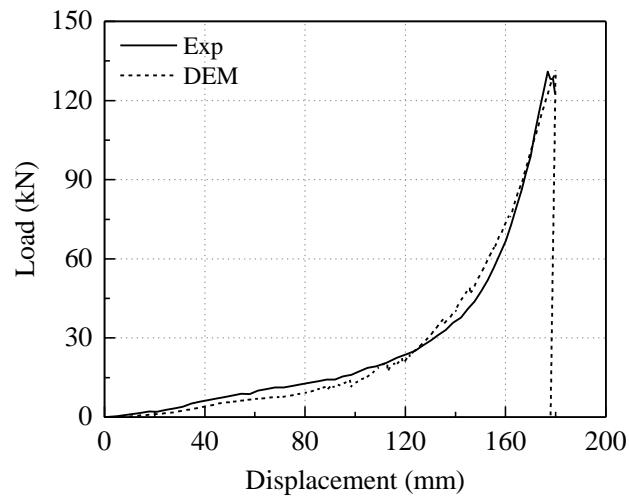


Fig. 4. Quasi-static tensile tests of a single wire ring and a group of wire rings: (a) schematic diagram of the experimental test setups (b) the DEM models.

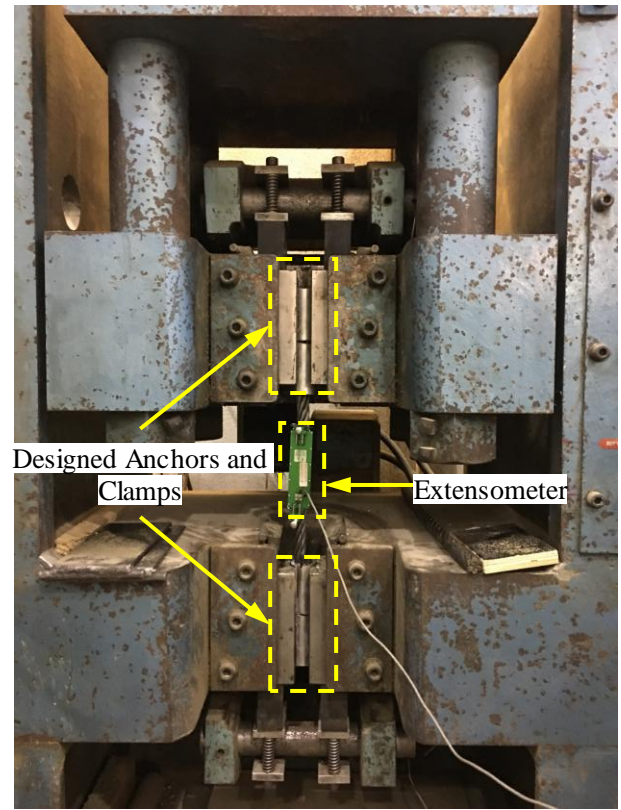


(a)

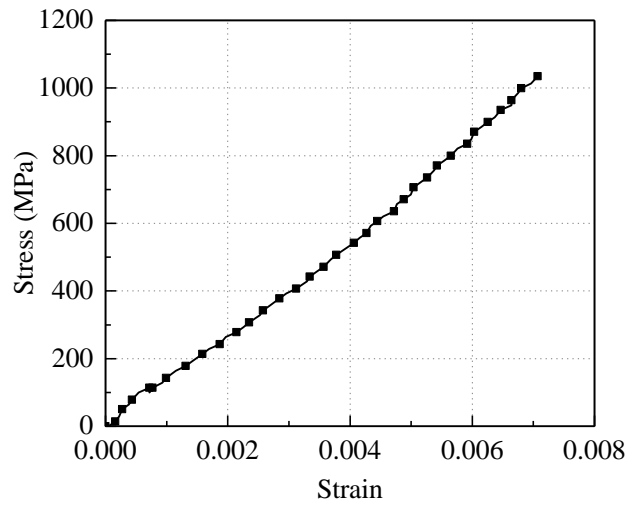


(b)

Fig. 5. Tensile test results comparison between the experiments and the DEM models: (a) a single wire ring (b) a group of wire rings.

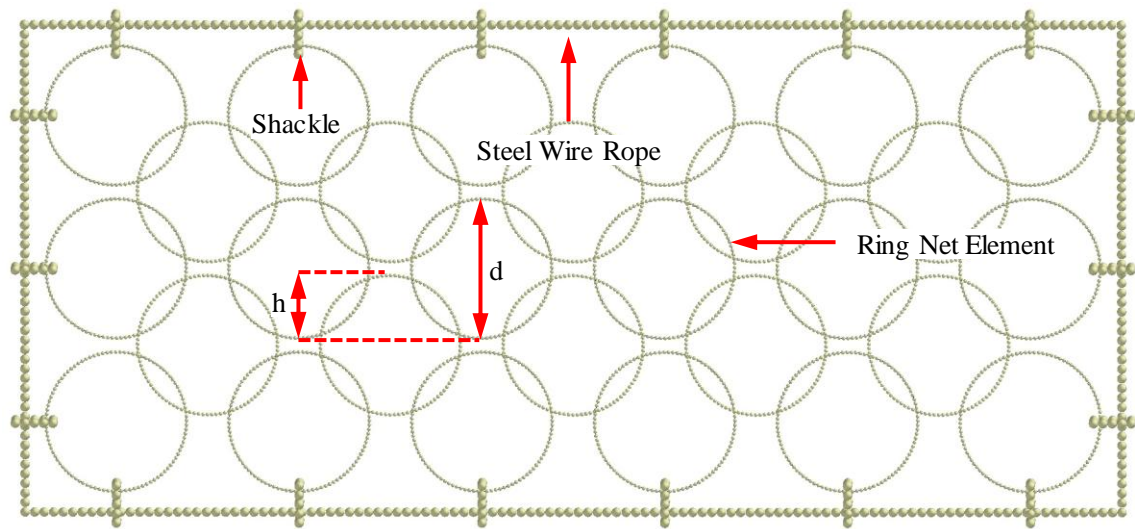


(a)

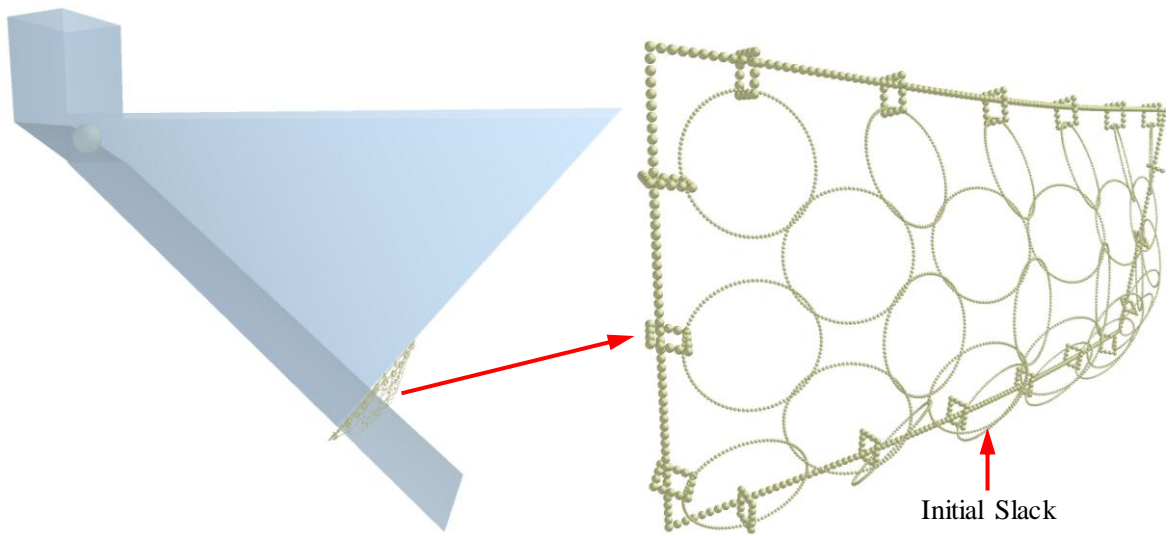


(b)

Fig. 6. Experimental tensile test of a steel strand cable: (a) test setup (b) stress-strain curve.

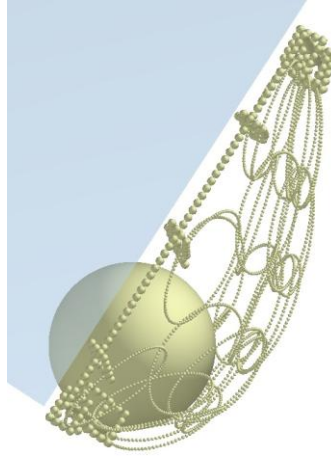
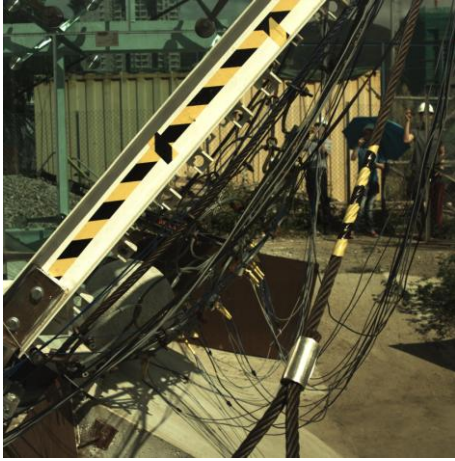


(a)

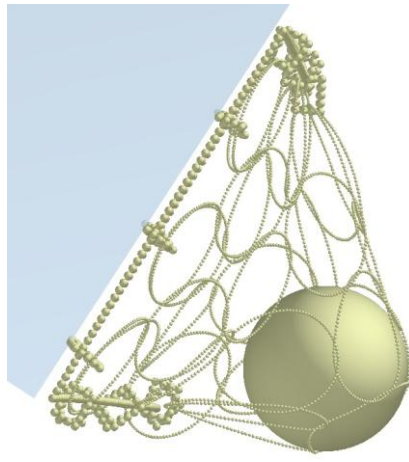


(b)

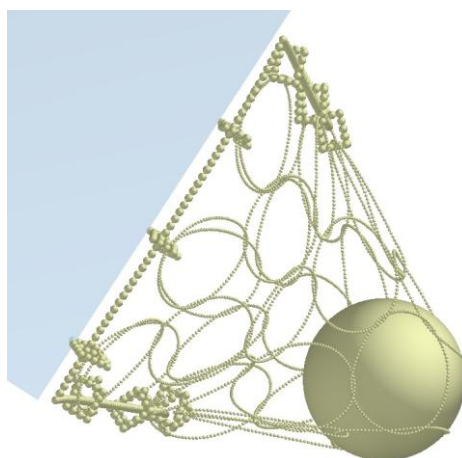
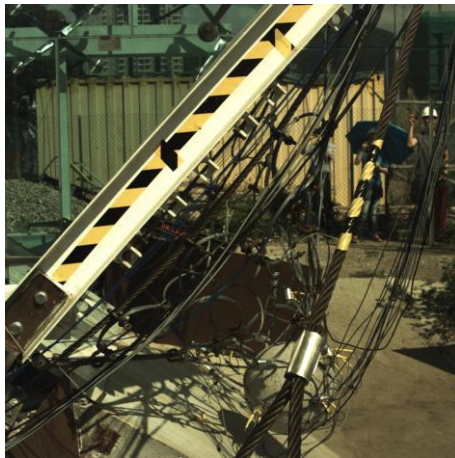
Fig. 7. Setup of the discrete element model: (a) the flexible ring net barrier at particle generation stage (b) model setup and the barrier with initial slack.



$t = 0 \text{ s}$

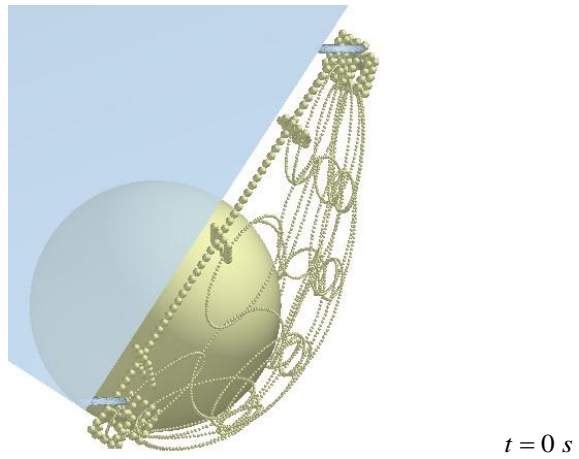


$t = 0.08 \text{ s}$

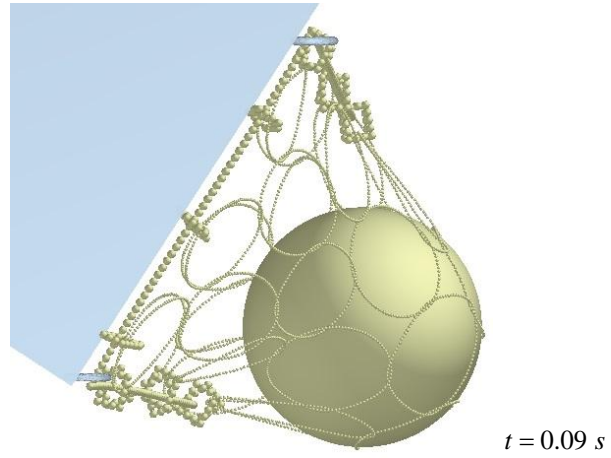


$t = 0.134 \text{ s}$

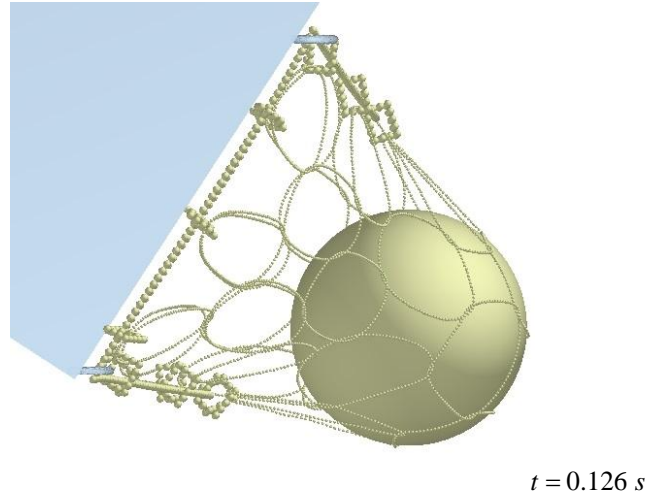
(a)



$t = 0 \text{ s}$



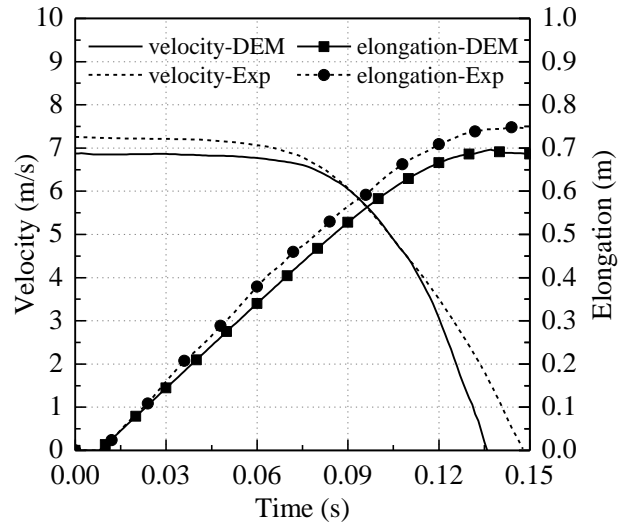
$t = 0.09 \text{ s}$



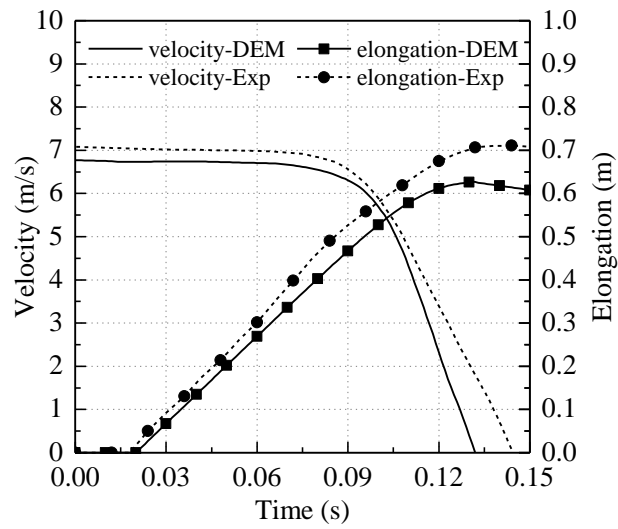
$t = 0.126 \text{ s}$

(b)

Fig. 8. Comparison of the experimental and numerical dynamic response of the flexible ring net barrier against rockfall impact: (a) test 1: boulder with 400 mm in diameter (b) test 2: boulder with 600 mm in diameter.

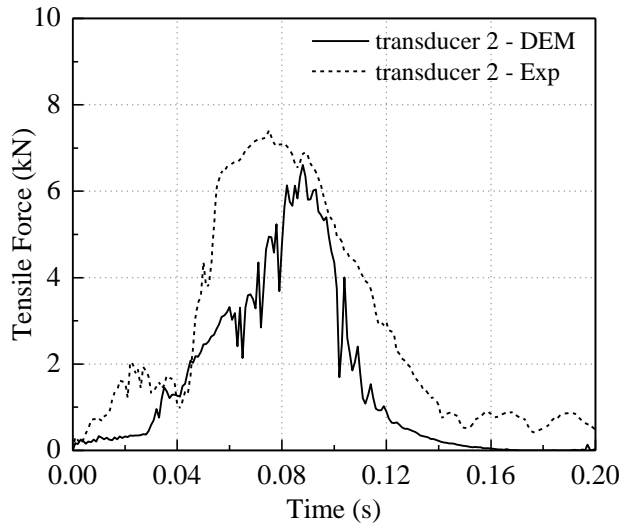


(a)

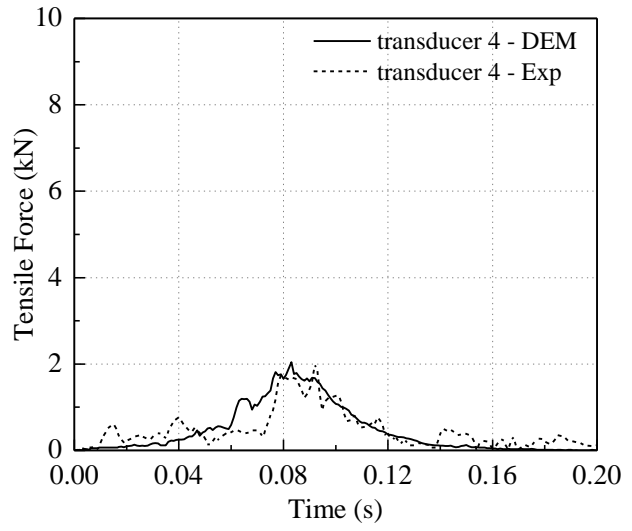


(b)

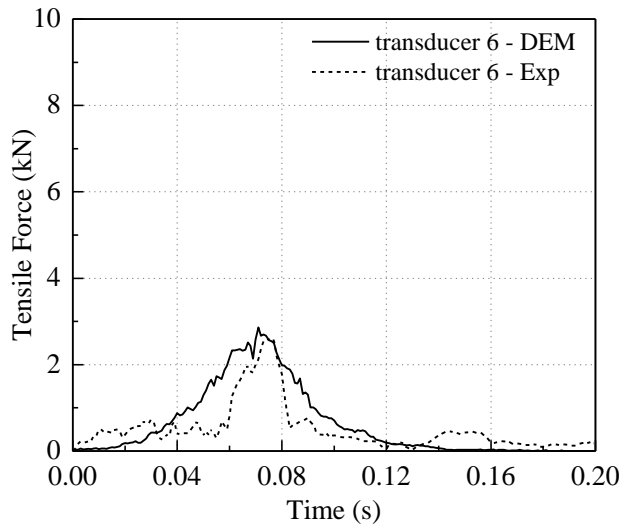
Fig. 9. The time evolution of the boulder velocity and net elongation for the two impact tests: (a) test 1: boulder with 400 mm in diameter (b) test 2: boulder with 600 mm in diameter.



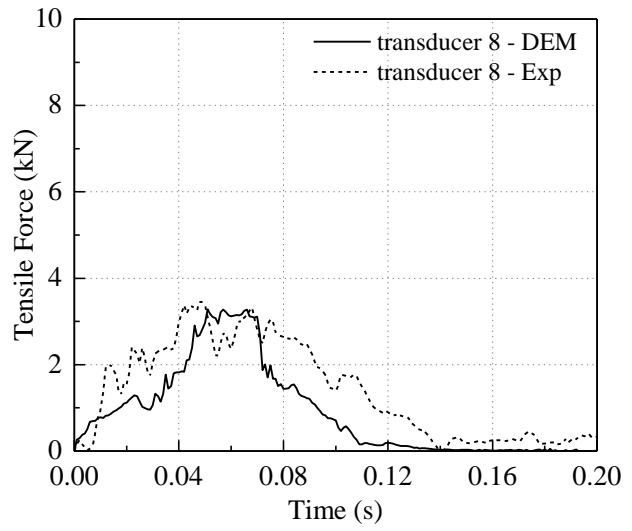
(a)



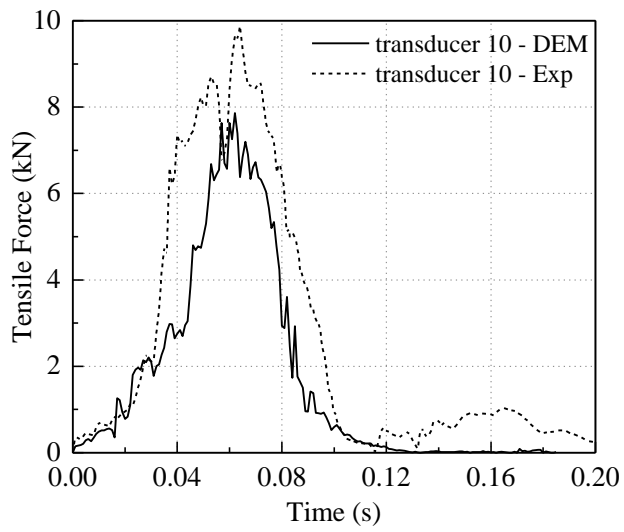
(b)



(c)

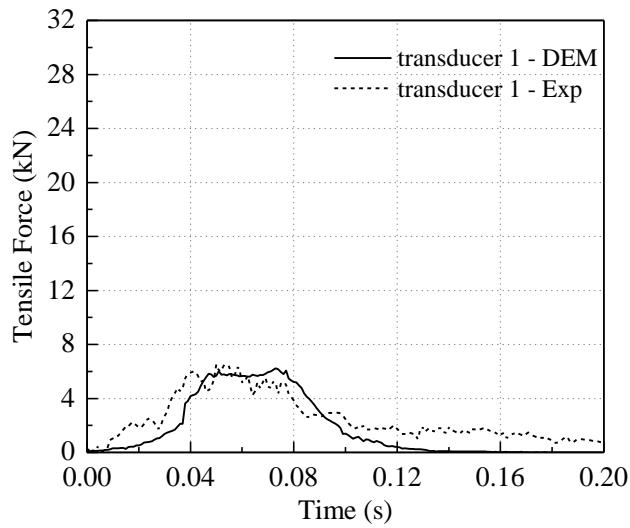


(d)

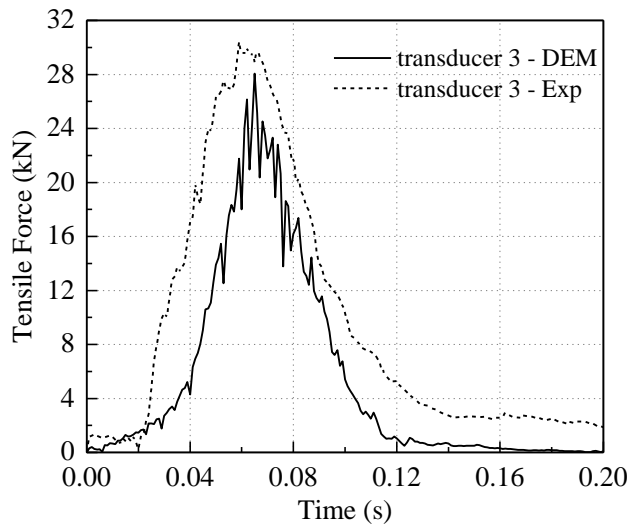


(e)

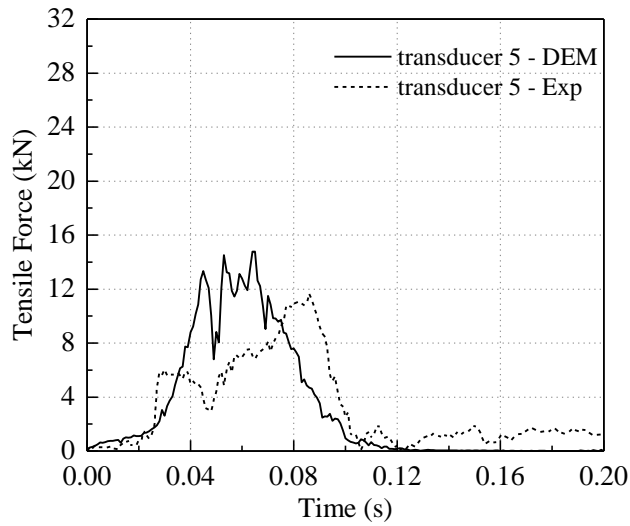
Fig. 10. Experimental and numerical time histories of the tensile forces at various positions of impact area for test 1.



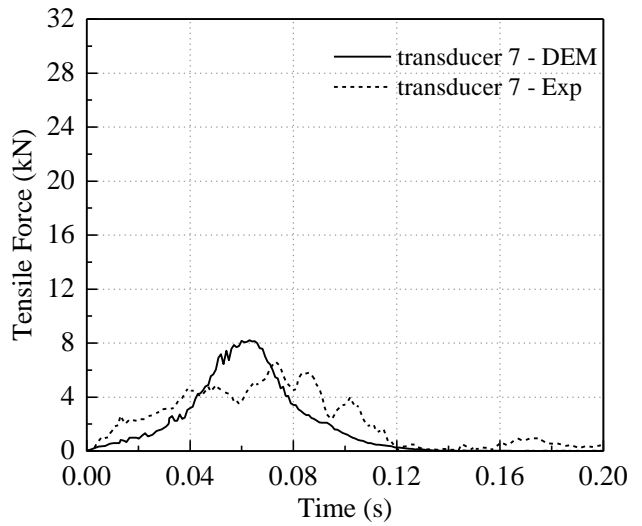
(a)



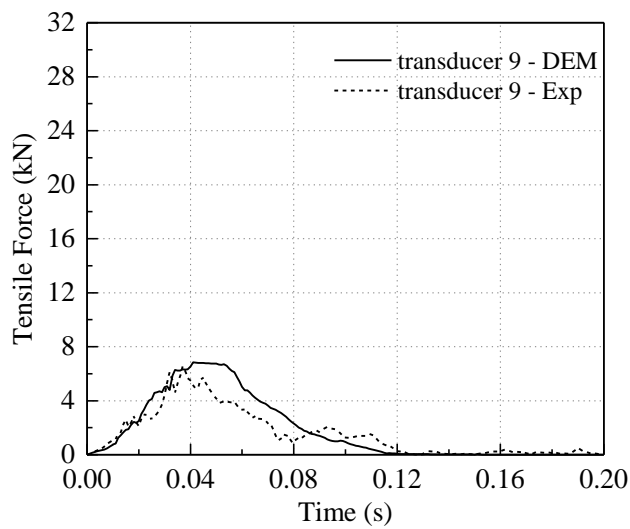
(b)



(c)



(d)



(e)

Fig. 11. Experimental and numerical time histories of the tensile forces at various positions of impact area for test 2.

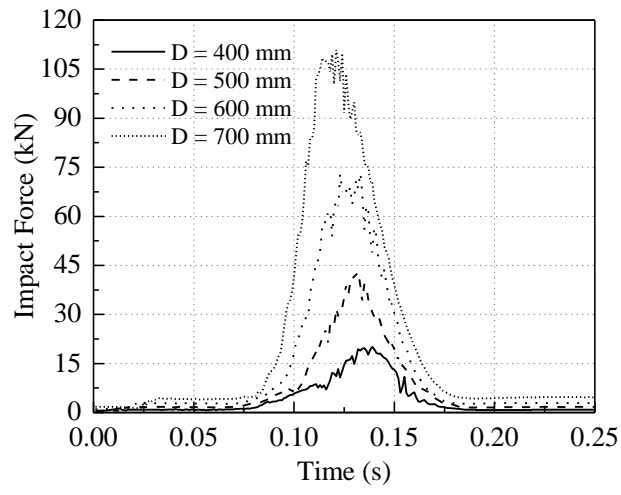


Fig. 12. Effect of the boulder size on impact force.

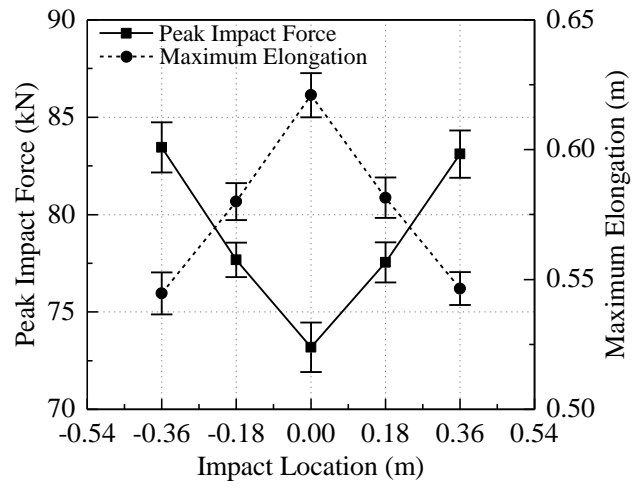


Fig. 13. Effect of the impact location on peak impact force.

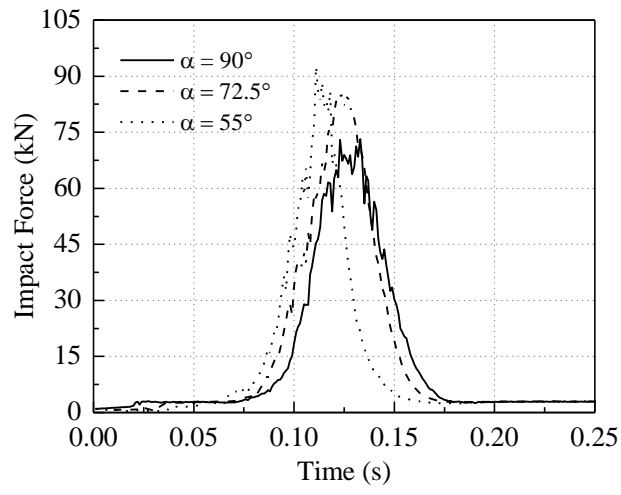


Fig. 14. Effect of the angle between the barrier and slope on impact force.

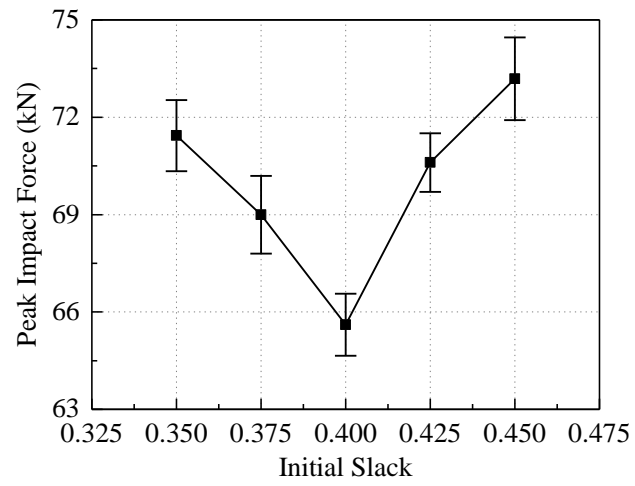


Fig. 15. Effect of the initial slack of a ring net barrier on peak impact force.